JOURNAL OF GEOPHYSICAL RESEARCH, VOL. 106, NO. E8, PAGES 17,609–17,621, AUGUST 25, 2001

The MVACS Robotic Arm Camera

H. U. Keller, H. Hartwig, R. Kramm, D. Koschny, W. J. Markiewicz, N. Thomas, and M. Fernades

Max-Planck-Institut für Aeronomie, Katlenburg-Lindau, Germany

P. H. Smith, R. Reynolds, M. T. Lemmon, J. Weinberg, R. Marcialis, R. Tanner, B. J. Boss, and C. Oquest

Lunar and Planetary Laboratory, University of Arizona, Tucson

D. A. Paige

Department of Earth and Space Sciences, University of California, Los Angeles

Abstract. The Robotic Arm Camera (RAC) is one of the key instruments newly developed for the Mars Volatiles and Climate Surveyor payload of the Mars Polar Lander. This lightweight instrument employs a front lens with variable focus range and takes images at distances from 11 mm (image scale 1:1) to infinity. Color images with a resolution of better than 50 μm can be obtained to characterize the Martian soil. Spectral information of nearby objects is retrieved through illumination with blue, green, and red lamp sets. The design and performance of the camera are described in relation to the science objectives and operation. The RAC uses the same CCD detector array as the Surface Stereo Imager and shares the readout electronics with this camera. The RAC is mounted at the wrist of the Robotic Arm and can characterize the contents of the scoop, the samples of soil fed to the Thermal Evolved Gas Analyzer, the Martian surface in the vicinity of the lander, and the interior of trenches dug out by the Robotic Arm. It can also be used to take panoramic images and to retrieve stereo information with an effective baseline surpassing that of the Surface Stereo Imager by about a factor of 3.

1. Introduction

The Robotic Arm Camera (RAC) is part of the Mars Volatiles and Climate Surveyor (MVACS) integrated payload (Principal Investigator, D.A. Paige) of the Mars Polar Lander (MPL). As the name expresses, the RAC is located at the end of the Robotic Arm (RA) [*Bonitz et al.*, this issue] and is used to choose and document the acquisition of surface and subsurface samples using the RA scoop. MPL was launched on January 3, 1999, and was intended to land on the layered terrain near the south pole of Mars on December 3, 1999. For an overview of the mission see R. W. Zurek et al. (manuscript in preparation, 2000). The optical concept of the RAC is based on a design by the University of Arizona group around P. Smith [*Reynolds and Hartwig*, 1997]. The compact mechanical design originates at the Max-Planck-Institut für Aeronomie (MPAE), where it was built. The RAC uses the same charge-coupled device (CCD) detector array as the Surface Stereo Imager (SSI) (for a description, see *Smith et al.* [this issue]). The read out electronics is common to both instruments (supplied by MPAE).

The science objectives of the RAC are summarized below. A detailed description of the camera follows, and its calibration and specific image-processing algorithms are discussed in the following sections. Sample images are provided to illustrate the expected performance.

Copyright 2000 by the American Geophysical Union.

Paper number 1999JE001123.
0148-0227/00/1999JE001123$09.00

2. Science Objectives

The top level science objectives of the MVACS payload are described by D.A. Paige et al. (manuscript in preparation, 2000). The close-up imaging capability of the RAC, providing a scale of resolution of 23 μm pixel^{-1}, and its mobility on the 2 m long RA permit a detailed investigation of the lander surrounding surface and subsurface. The illumination system of the RAC can be used for coarse characterization of the reflection properties of the surface and materials if different spectral features can be separated.

Plate 1. Robotic Arm Camera (RAC) flight model showing front face with optical entry window and illumination lamps.

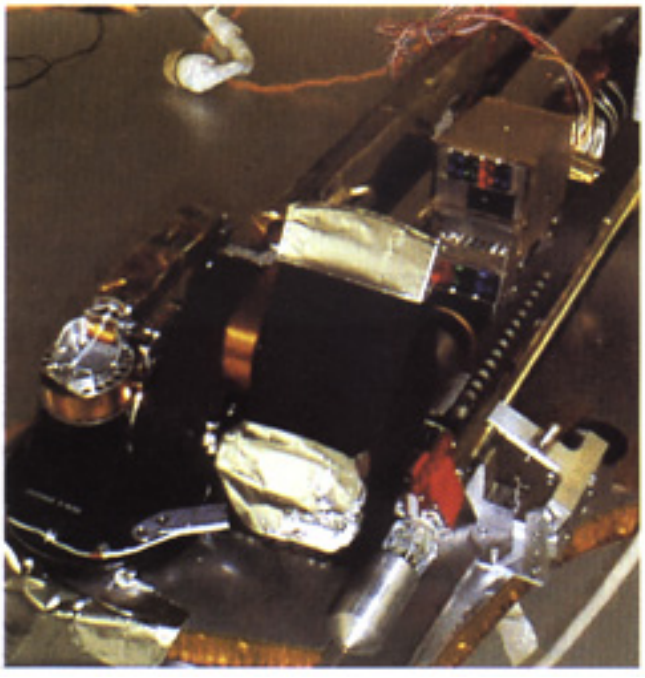

Plate 2. RAC integrated in its flight position on the Robotic Arm. The RA scoop is in the center of the image.

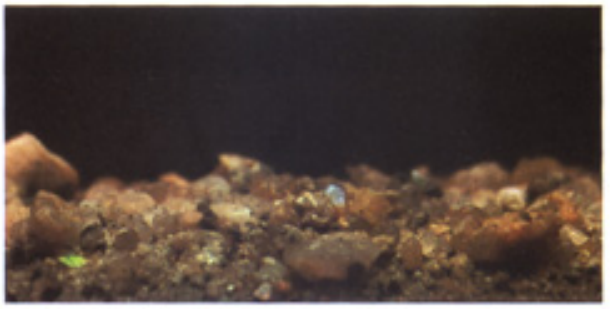

Plate 3. Fine soil at close focus, 25 μm pixel^{-1} (12.5 cm field of view).

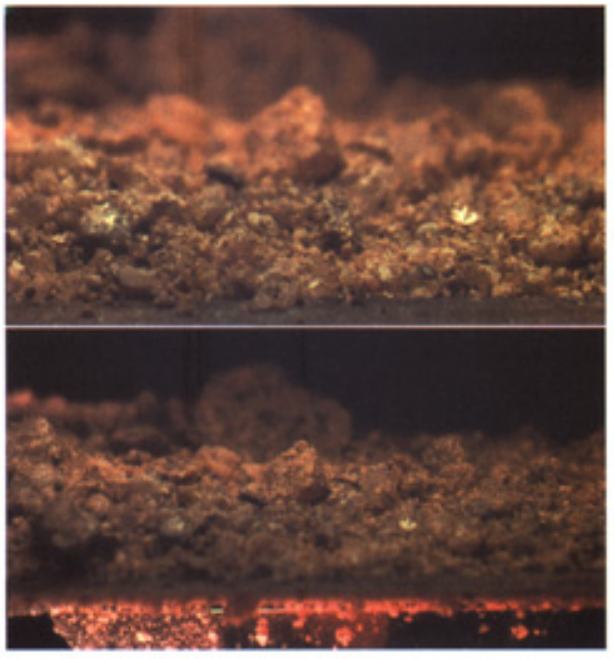

Plate 4. Effect of the focal distance. (top) Close focus is at 11 mm distance, and (bottom) the farther focus is at 16 mm distance (46 μm pixel^{-1}, 23.5 mm field of view).

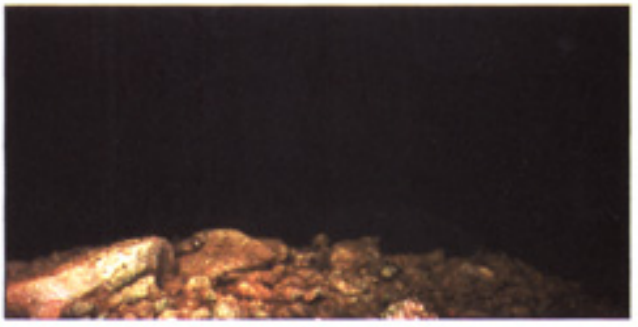

Plate 5. Image of the scoop tilted back. In-focus material is 54 $\pm$ 10 mm distant. The resolution is 122 μm pixel^{-1} and the field of view is 62.5 mm.

The RAC will perform the following functions: (1) be instrumental during the search for near-surface ground ice while digging trenches; (2) characterize the physical properties (grain size, clumpiness, heterogeneity, etc.) of the soil samples to be analyzed by the Thermal and Evolved Gas Analyser (TEGA) [*Boynton et al.*, this issue]; (3) document the origin of the soil samples; (4) help to quantify the abundance of volatile-bearing minerals in the Martian soil; (5) search for seasonal and climate records in the form of fine-scale layering in the trenches and near-surface materials; (6) help to determine and analyze the weathering processes of surface rocks; (7) assist in the mineralogical and geological characterization of the landing site; and (8) observe and quantify surface and sub-surface condensation and sublimation processes of volatiles such as water. The high resolution images from the RAC, together with stereo images from the SSI, will provide the capability to investigate the near surroundings of the lander with an unprecedented dynamic range of scale of the order of 10^5.

The RAC can also be used to generate panoramas of the surroundings of the lander by taking advantage of its larger (about a factor 8) of field of view (FOV) as compared to SSI. Color panoramas will, of course, not be possible due to the lack of filters. It will, however, be possible to combine overlapping images to extract stereo information. The effective stereo base (geometric separation of aperture divided by resolution ratio) could be 3 times larger than that of SSI, increasing the distance of measurements by the same factor. In essence, the area around the lander for which stereo information can be obtained could be increased by an order of magnitude. However, because of the restriction on the RA joints, the RAC will not be able to image the full 360° panorama.

The macro images with an imaging scale down to 1:1 onto a detector element of 23 μm will reveal the fine structure and texture of the diverse mineralogical units. Microscopic scales that will show, for example, settled dust grains will have to wait for the following lander mission of the Mars Surveyor program, when an optical and an atomic force microscope are flown as part of the Mars Environmental Compatibility Assessment (MECA) payload (mars.jpl.nasa.gov/2001/lander/meca/index.html). It is obvious that the unprecedented resolving power of the RAC will provide major scientific return, making the RAC one of the key elements of the scientific payload of MPL.

3. Instrument Description

3.1. Overview

The RAC (Plate 1) is located on the lower side of the forearm of the RA just behind the wrist and close to the scoop so that the digging blade of the scoop can be put within minimum focus range (see Plate 2). The RA and its operation are described in the accompanying paper by *Bonitz et al.* [this issue]. The volume of the camera body is $78 \times 62 \times 61 \mu m^3$ with the upper illumination lamp assembly increasing the total length by another 34 mm. The total mass is 380 g including the Sensor Head Board (SHB), two mechanisms, and lamp assemblies. The mechanical assembly consists of a very lightweight frame that serves as an optical bench. The size of the RAC is driven by the existing detector package and SHB that were originally designed for the Descent Imager/Spectral Radiometer (DISR) camera on board the Huygens Probe of the Cassini mission [*Tomasko et al.*, 1997]. The same detector package and SHB are also used in the SSI. The RAC is tested to operate in the temperature range between 160 and 320 K. The drive motors have to be heated to their operational temperature above 210 K.

The same CCD detector array as used for the SSI is a frame transfer device with an optical active surface of 512×256 pixels. Therefore the field of view (FOV) of the RAC is rectangular, whereas the SSI places both the images from the right and left eye onto the same detector surface (256×256 pixels for each eye).

Originally, the RAC was conceived as a fixed focus camera with a working distance of 115 mm, yielding a scale of 4:1 (IFOV = 100 μm). A rigorous redesign decreased the required mass and volume resources so much that a variable focus driven by a motor could be implemented into the RAC. The minimum focus distance is 11 mm in front of the window where an image scale of 1:1 is achieved. At infinity the resolution of the RAC is 1.85 mrad pixel^{-1}, somewhat less than the resolution of the SSI at 1 mrad pixel^{-1}. This corresponds to a total FOV of 54° × 27° for the RAC.

The RAC consists of the following subsystems (see Table 1): (1) optical bench/frame and Sensor Head Board with CCD detector, (2) double Gauss lens with lens cell, (3) lens focusing mechanism with stepper motor and reference switch, (4) protective cover with mechanism, stepper motor, and reference switch, (5) upper and lower lamp assemblies, (6) two temperature sensors, and (7) a protective shell. The SHB is identical to those developed for the Imager for Pathfinder and MVACS-SSI and thus will not be described here [see *Kramm et al.*, 1998]. The drive motors, front lens assembly with cover, and the upper and lower lamp assemblies are provided by the University of Arizona.

3.2. Optomechanical Layout

The combination of a 12.5 mm effective focal length (e.f.l.) lens and the 1:1 imaging requirement leads to a geometry where the minimum object distance from the CCD is about 50 mm and the lens position varies between 12.5 and 25 mm from the CCD. Given the length of the lens cell body and the need for a safety distance

Table 1. Robotic Arm Camera (RAC) Subsystem Specifications

Item	Specification
	CCD Detector
Make	Loral (now Lockheed Martin Fairchild Systems)
Type	front illuminated, frame transfer, antiblooming
Image section size	512 × 256 pixels
Pixel size	23 × 23μm (including 6 mm antiblooming structure)
Readout time	16μs per pixel, 2 s per image
Exposure times	0 to 32 s in steps of 0.5 ms, autoexposure selectable
Readout noise	< 10 el rms
Full well	1.1 10^5 el
A/D conversion	12 bit per pixel (0 - 4095 DN)
Electronic gain	26 el/DN
S/N ratio	~ 350 (maximum)
	Camera
Focal length	12.5 mm, variable focusing
Scale	from 0.9 at 11 mm object distance to 1.8 mrad pixel^{-1} at infinity
FOV	54° × 27° for focus at infinity
Broad band filter	IR cut off at 700 nm
Illumination (two assemblies)	lamp colors: blue, green and red

A/D, analog to digital; DN, digital number; FOV, field of view.

in front of the RAC, a very compact design of the RAC assembly in front of the CCD is needed.

The optical bench essentially consists of three walls or bulkheads (front, center, and rear) which are braced against each other by two side frames (left and right). The volume between the front bulkhead and the center accommodates all optical and mechanical subsystems, while the volume between the center bulkhead and the rear houses the SHB electronics, with two connectors mounted to the rear bulkhead. The bulkheads are basically $60 \times 60 \times 5$ mm^3 aluminum plates which are highly sculpted with pockets and flanges in order to keep mass to a minimum (see Figure 1).

The SHB is mounted with its three hard points flush against the rear side of the center bulkhead, with the CCD protruding into a pocket in the bulkhead. The sensitive area is illuminated through a rectangular cutout from the lens side.

3.3. Lens System for Variable Focusing

A 12.5 mm e.f.l. double Gauss lens design stopped down to a relative aperture of $f/11.2$ was selected to achieve the desired combination of resolutions and working distances. Titanium was used in cell construction to provide a close match in thermal expansion with the glass, thereby permitting operation over the wide temperature range. An infrared-blocking filter window with a cutoff wavelength at ~ 700 nm is mounted in the cell ahead of the lens to limit longer-wavelength radiation and improve the system signal-to-noise (S/N) ratio as explained below.

The RAC filter window is a gradual cutoff filter that reduces the red light transmission as well as blocking infrared (IR). Transmission of the filter window is shown in Figure 2. The IR blocking of the filter will give

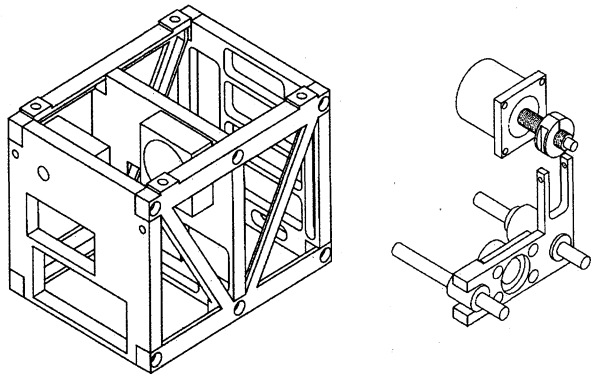

Figure 1. (left) RAC frame (optical bench) and (right) focusing mechanism.

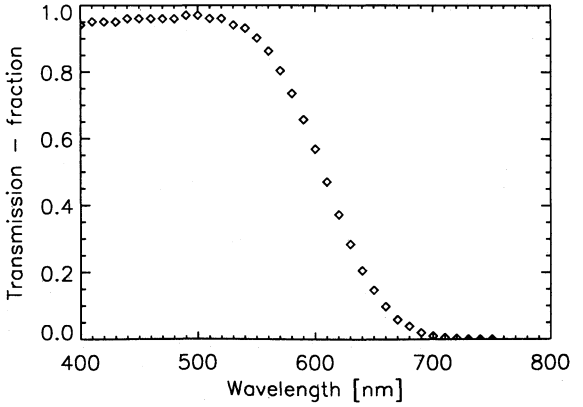

Figure 2. Transmission of the CCD window IR blocker.

a significant improvement in the modulation transfer function (MTF) for daylight imaging by eliminating the point spread function (PSF) spreading due to diffusion in the silicon from IR generated electrons. The filter will also give a view of the scene that would be more representative of human vision.

The reduction in red transmission was done to improve the S/N ratio of imaging with the blue and green lamps. A reduction in the red transmission for ambient light imaging will not affect S/N ratio; it will just increase exposure times. While imaging with the lamps on will be done in shadow, the stray light from the sky limits the exposure time. Since this light is predominately red, reducing the red responsivity by half doubles the exposure time. Doubling the exposure time gives twice the signal from the blue and green lamps. To remove the stray light from the image, the same scene will be imaged with lamps on and then with lamps off. Subtraction of the two images will remove the stray light. Since the noise is predominately from the stray light, and is approximately constant, doubling the signal with constant noise doubles the S/N ratio. This was needed to achieve a minimum S/N ratio with the blue and green lamps.

3.4. Focusing Mechanism

The lens in its cell is mounted to a translation stage which allows its position along the optical axis to be changed from infinite conjugate ratio to 1:1. The mechanism consists of a pair of cylindrical guide shafts with a diameter of 4 mm that bridge the span between the front and center bulkheads (see Figure 1). The main bearing of the translation stage consists of two linear ball bearings in series on one shaft while a single linear ball bearing held in the fork end of the stage slides along the other shaft and thus prevents rotation of the stage. Above the plane defined by shafts is the drive lead screw with a diameter of 5 mm and pitch 0.5 mm mounted directly onto the shaft of the stepper motor. This lead screw moves a VESPEL nut which is held by a forked out-of-plane extension of the stage. Since this mechanism must be tolerant of the wide temperature range to be expected, great care is taken to avoid overconstraining the guiding system. With a motor step angle of 30 (12 steps per revolution or 24 steps/mm) the focusing step increment is 0.04167 mm. Total movement range is 13.0 mm or 312 steps. The design of the drive allows it to be run against the stops at the extremes.

3.5. Reference Switch of the Focusing Mechanism

In order to initialize the motor step counter after switch-on, there is an optical (IR) interruptor reference switch mounted to the fixed part of the mechanism below the stepper motor. A vane on the moving stage interrupts the IR beam at a fixed point within the travel range. The emitter and detector together with their respective resistors are integrated onto a small three-dimensional printed circuit structure made of Al2O3 ceramic. The detector output switches from "low" to "high" when the vane interrupts the beam. At switch-on the mechanism control software can read from the switch status which side of the reference position the stage is located: "low" means the stage is farther away from the CCD than the reference position, and "high" indicates that the stage (and the lens) is closer to the CCD than the reference switch position. Appropriate commands move the lens into the reference position.

3.6. Cover Mechanism

The protective cover has a full-size sapphire window to protect the filter window against scratches from flying dust and dust or frost depositions. Small conductive carbon fiber brushes along three sides of the cover remove particles and static charge from the face of the filter window during each actuation. The cover is rotated to the open position by an eccentric driven by a stepper motor. An eccentric pin on the motor shaft (eccentricity 3.5 mm) engages a slotted arm fitted to the inside end of the shaft the cover is rotating about. The motor shaft and the cover shaft are offset by 5 mm.

The same type of reference switch as in the focus drive is used: a narrow rotating vane interrupts an IR beam exactly in the closed position (output state is "high"). As soon as the cover begins to open, this changes to "low". Any incomplete opening of the cover must be deduced from the actual image.

3.7. Temperature Sensors

Besides the temperature sensor integrated on the CCD chip, two extra AD 590 sensors are bonded to the rear body of each of the drive motors. Monitoring of these sensors will allow warming the motors to the minimum temperature required by the grease lubricant in their bearings and to prevent overheating due to extended operation. The steadystate temperature of the camera body can be read from the SHB temperature sensor.

3.8. Protective Shell

The optical bench assembly is enclosed by a two-part protective shell made out of 0.5 mm aluminium sheet: a U-shaped hood and a flat bottom cover. These are attached by countersunk M2 screws so there are no protruding screw heads. The sheet material is drawn below the screw heads to obtain additional formlocking for extra stability. The edges are sealed by strips of polyamide adhesive tape in order to make the enclosure dustproof. Pressure equalization will be achieved through a pair of sintered stainless steel filter discs located at the rear, at the side of the connectors. Surface treatment of the external faces is chromate conversion (IRIDITE). Thermo-optical properties consist of solar

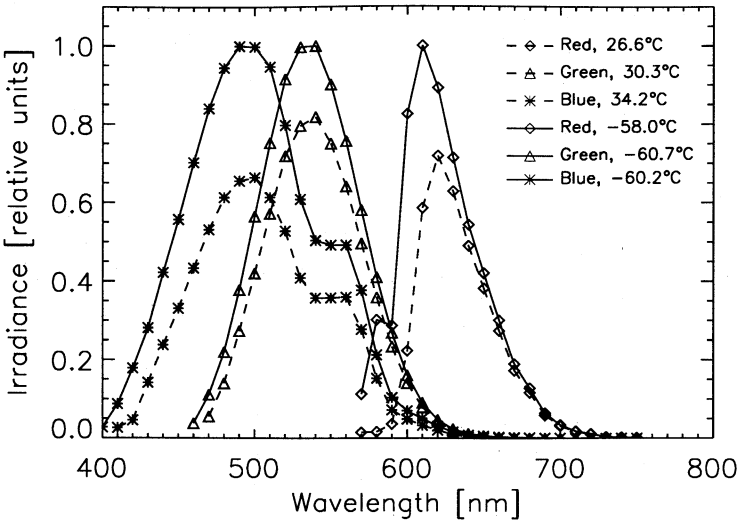

Figure 3. The spectral characteristics of the RAC lamps.

absorptivity $a = 0.64$ and hemispherical thermal emissivity $e = 0.05$ (at room temperature).

3.9. Illumination System

The requirements to cover the closest object distance of the 1:1 macro position and also to illuminate the rear of the scoop or the bottom of the trench are difficult to meet. The location and properties of the illumination system are critical to the performance of the RAC. The successful superposition of images taken with different colors crucially depends on the illumination geometry that has to be as similar as possible for all lamp sets.

Two lamp assemblies (lower and upper) are mounted to the front face (see Plate 1). The lower assembly comprises two red, two green, and four blue incandescent bulbs in linear faceted reflectors behind color filter windows and is located below the filter window of the camera. The upper assembly above the filter window is protected by a sloping glass window and consists of a series of individually aligned downlooking lamps (two red, two green, and four blue) which provide illumination of the RA scoop leading edge and contents even in the close-up position.

The spectral characteristics of the lamps are shown in Figure 3 and Table 2. The red lamp shows a spectral, center wavelength shift with temperature because of the temperature coefficient of the red filter glass material.

Table 2. RAC Lamp Characteristics at -60 C as Measured Through the 613 nm IR Block Filter

	Peak Wavelength, nm	FWHM, nm
Red	611	50
Green	535	78
Blue	495	104

FWHM, full width at half maximum.

All three lamps increase in irradiance at lower temperatures due to the reduction in cable resistance at lower temperatures and the resultant increase in lamp voltage. The lamps reach their normal voltage at −90°C.

3.10. CCD Detector Array

The CCD was originally developed by Loral (now Lockheed Martin Fairchild Systems) for space application under a contract by the Max-Planck-Institut für Aeronomie within the Cassini DISR project. The CCDs used for SSI and RAC are produced by an improved production process applying a gold rather than aluminium coating for grounding of the substrate die.

The CCD is a front side illuminated device employing buried channel technology with two-phase multipinned-phase (MPP) clocking. The pixel spacing is 23 μm in both directions; however, 6 μm in line direction of each pixel are covered by an antiblooming structure to remove excess charge in case of overexposure. The storage section of the frame transfer device of 512 × 256 pixels is covered by an opaque aluminium mask. The rapid line transfer after an exposure of typically 100 ms takes 1 ms total (4 μs per line) so pixel transfer smear is almost negligible. The full well capacity of each pixel is 1.5×10^5 electrons.

3.11. Read Out Electronics

The SHBs of both cameras are connected via long (up to 4 m) electrical lines to the CCD Readout Board (CRB) located inside the central electronics box of the lander. This board accomodates the analog signal chains with correlated double sampling, a sample and hold amplifier, a 12 bit analog to digital (A/D) converter, a clock driver, a power converter, and a digital control unit with a parallel interface to the experiment processor via the frame buffer board (see description of SSI by *Smith et al.* [this issue]. Further details of the

CCD and electronics are given in the paper by *Kramm et al.* [1998].

3.12. Operations

The RAC is controlled through sequences of uplinked commands, sharing most of the software with SSI. Extensive exposure control is available. Images can and will be data compressed using a modified JPEG algorithm developed at the University of Braunschweig [*Rüffer et al.*, 1995]. The data volume of the RAC is large compared to the daily transfer. One full image contains 512 × 256 × 12 bits or more than 1.5 Mbit. The very limited depth of focus of macro images at close range requires about 10 images to cover the full depth of soil samples in the scoop. This amounts to a total data volume comparable to the "daily allowance" for the RAC. On each exposure only a minor part of the image is in focus, and therefore only the corresponding pixels contain useful information. Specific algorithms and methods of onboard image analysis need to be applied (see section 6) to reduce the raw data volume considerably. Spectral information needs another factor of 3 to cover exposures with the three different lamp sets.

The RAC will also be extensively used to support the operation of the RA and other scientific investigations, such as selection and characterization of soil samples for TEGA analysis, the soil temperature probe, and the magnet investigation. After landing, the immediate environment including the lander foot pads will be investigated using the RAC to characterize surface properties.

4. Calibration

4.1. Overview

The parts of the calibration mainly relating to the properties of the CCD are similar to procedures used for the Imager for Mars Pathfinder (IMP) camera [*Smith et al.* 1997] and SSI [*Smith et al.*, this issue] and will be only briefly touched upon here. Analysis of the depth of focus as a function of the object distance, the focus variation as a function of the drive motor steps, and the focus and imaging errors across the FOV are tasks that are applicable to the RAC only.

4.2. CCD Properties

The CCD is a front side illuminated frame transfer device with antiblooming structure consisting of a (512 active + 16) column by 256 line imaging section and a (512 active + 16) column by 256 line storage section covered by a metal mask. Each line from the serial readout register contains four null pixels (the "null strip") providing system noise information, eight dark pixels (the "dark strip") measuring dark current, 512 active pixels, and four null pixels again. These dark current strips are used to scale dark current corrections on board using the line-by-line ratios.

The pixel charge capacity of the 23 × 17μm active pixel surface is dependent on the potential of the antiblooming gate barrier and was adjusted for a full-well value of 105,000-110,000 electrons for the RAC CCD (# 142). For a full-scale range of 110,000 electrons with the 12 bit analog-to-digital (A/D) converter (ADC), a system gain of 26.9 electrons per digital number [DN] is required.

Table 3 shows measured values for several other CCD parameters at three temperatures. Dark current is per pixel for an array average and an exposure time of 2s. Readout noise is at the CCD subsystem level for the nominal readout rate of 16 μs pixel^{-1}. The maximum linearity error (relative linearity) is shown. The vertical charge transfer efficiency (CTE) is measured at a signal level of 10,000-20,000 electrons at a clocking rate of 4 μs/line. Uniformity refers to the number of pixels whose photoresponse deviates by more than ±4% from the average photoresponse of the array at the signal level of 50,000-70,000 electrons, using a nominal 3200K tungsten-halogen light source with a daylight filter (such as Scott BG26). A maximum of 1000 blemished pixels (pixels that do not meet the array performance specifications) may be exempted.

4.3. Flat Fielding

The flat field frame corrects the responsivities of individual pixels to a common reference for accurate radiometric measurements and to remove visible responsivity artifacts. The flat fields generated are further divided into ground flat fields and the flight flat fields. The

Table 3. CCD Parameters Determined at Different Temperatures

Parameter	283 K	253 K	193 K
Dark current (2 s), electrons	488	30	10
Noise (rms), electrons	22.6	12.4	8.5
Full well, electrons	109,400	108,400	106,000
System gain, el/DN	26.8	26.5	25.9
Linearity error, %	< 0.25	< 0.5	< 0.5
(Vertical) CTE	0.999996		0.9999995
Uniformity* (> 4%)	1 pixel		1 pixel

CTE, charge transfer efficiency.
*See section 4.2.

ground flat fields are used for calibrating data from the spacecraft that have not been flat fielded on board the spacecraft. The flight flat fields are used to flat field images on board the spacecraft before JPEG compression to enhance compression efficiency and accuracy.

The accuracy of the responsivity corrections across the focal plane CCD detector array depends on the noise of the image, a knowledge of the pixel-to-pixel responsivity variation, and the intensity variations caused by the imperfection of the optical elements. Major contributors within the RAC are the crisscross pattern of the silicon wafer caused by the polishing of the CCD (high frequency, small amplitude) and the falloff (vignetting) at the corners of the chip, varying from 14 to 50% between close and infinity focus. The pixel-to-pixel change in responsivity is small. The achieved accuracy is estimated to be around 1%.

The ground flat field data exist for focus steps of 0, 87, 125, 153, 177, 198, 217, 234, 250, 265, 279, 292, and 300, each with the RAC cover window up and down. Each image has a SNR of > 200. Data for focus steps 306 and 312 will be extrapolated from the Mars Surveyor 2001 RAC and the above data set. At the time of the flat field testing for MPL RAC it was not possible to run the camera beyond 300 steps because of a software limitation. Each image is the average of 10 images taken in a large integrating sphere. Each image has been dark and shutter corrected. The images are in VICAR format for use with the MPL image calibration program.

The flight flat fields are stored on board the spacecraft in compressed form and decompressed for use. The flight flat is generated to remove spatial transients in the images before JPEG compression. Since there is only Electrical-Erasable-Read-Only-Memory space for one flat field of 8 bit depth, the flight flat field was generated by averaging the flat fields for the 300 step focus flat. The 300 step flat is chosen because this focus position needs the most flattening.

4.4. Absolute Calibration

The response of the camera to lamp illumination of a SPECTRALON target is measured over temperature and for a variety of focus distances. The resulting data are then combined with the spectral data and the absolute calibration of the CCD to determine an absolute irradiance from the lamps. Because of test equipment problems and time limitations, the lamps were measured only down to $-60°$C. Extrapolation of the data set from tests of a spare set of lamps will extend this data to $-100°$C.

Because of the larger relative aperture of the RAC and the fact that it operates as a broadband instrument, the responsivity of the RAC is significantly higher than that of the IMP and SSI. This will be important for acquiring good images of deep trenches dug by the RA and the rear portions of the scoop. The response of the camera to blue photons increases with a drop in temperature, whereas the response to near-infrared photons decreases. Midrange response around 550 nm is roughly constant with temperature. These effects will have to be accounted for when correcting RAC images.

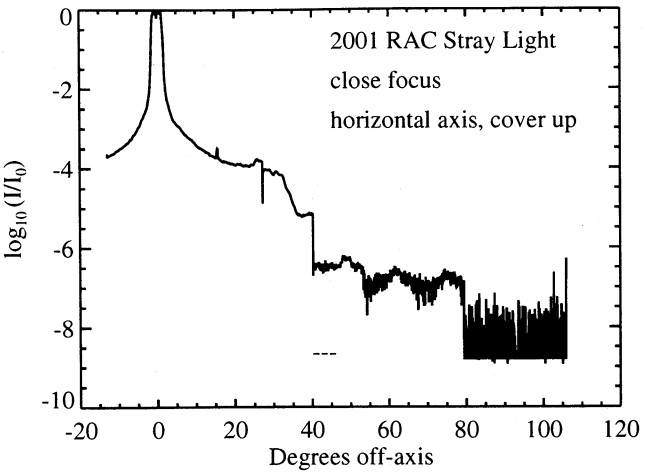

Figure 4. 2001 RAC stray light characteristics. See text for details.

4.5. Stray Light

The term "stray light" includes at least two components. The first is a general "fogging" of the image due to, for example, scattering by dust particles on the optical components (in particular, the camera window). The second component includes "ghost images" caused by multiple reflections within the camera optics. The goal of stray light calibration was to estimate or to place upper limits on both of these components, preferably as a function of wavelength.

Stray light data for the MVACS RAC were unfortunetaly contaminated by an extraneous light source, rendering them useless. To estimate the stray light properties of the MVACS RAC, the 2001 RAC had to be used. This camera is optically and mechanically very similar to the MVACS RAC. One stray light plot is shown in Figure 4. There are two distinct "regimes" in Figure 4. Out to about 40° off-axis, the main source of stray light appears to be internal reflections within the camera. The "notch" at 28° is due to a ghost image when the source is just beyond the field of view. Another one can be seen between 35 and 40°. Beyond 40°, individual point spread functions of dust and imperfections in the camera window become apparent. It should be noted that results shown in Figure 4 were obtained in the clean room. During mission operations both the cover window and the front camera window can be expected to be rapidly contaminated by submicron- to micron-sized dust particles from the onset of digging. These dust particles are efficient scattering centers. Therefore stray light during landed operations will be variable and more severe than the estimates provided here.

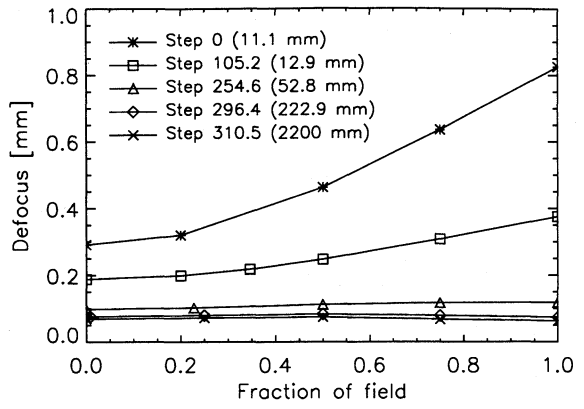

Figure 5. Defocus from the geometric focus to minimize the RMS spot size for various focus distances and off-axis points. The maximum off-axis point is the corner of the CCD.

4.6. Focus Model

The front lens of the RAC is moved by a stepper motor from the 1:1 image point (close focus) to infinity focus. This travel is 12.5 mm, and the lens moves in 300 41.7 μm steps. The actual camera has 313 positions, numbered from 0 to 312. Focus distance is defined from the front face of the camera (excluding lamps) to the object plane. Closest focus is 11.03 mm at step 0. Step 0 is also the initialization point for the focus motor. The RAC focus model correlates the step number to a particular focus distance.

To support the onboard autofocus and depth of focus algorithms, a set of standard focus positions was generated. These standard focus positions are spaced one depth of field apart; i.e., the far focus limit for one focus position would be the near focus limit of the next position. Depth of field at each focus position is calculated from a geometric blur criterion with the size of the blur set equal to the size of a pixel, or 23 μm. These focus positions start from step 0 and extend to the hyperfocus position at step 306. At this position the depth of field extends from about 280 mm to infinity. The positions of other useful intermediate focus points are also calculated. The focus model is developed by using an optical design and ray-tracing program (ZEMAX) to determine the lens-to-CCD spacing. Optimum focus is experimentally determined by moving the lens position to minimize the RMS spot size. This defines the lens-to-CCD distance at the step number found from the focus analysis. The model results for the standard focus positions are shown as Table 4. Some additional focus points are listed near the end of the table.

Minimizing the spot size produces a significant defocus as compensation for the small amounts of spherical aberration, astigmatism, and field curvature. The amount of defocus changes with focus distance, ranging from 0.29 mm at close focus to 0.07 mm at infinity focus (see Figure 5). Since the type and amount of aberrations change with focus distance and off-axis angle, the defocus correction is not a simple linear one. This small shift in the lens-to-CCD distance translates into

Table 4. Focus Distance for Standard RAC Depth of Field Steps, Hyperfocus, Infinity, and TEGA Focus Distances

Motor Step	Near Depth of Field*	Focus Distance	Far Depth of Field*	Scale, mrad pixel^{-1}	mm pixel^{-1} at Object	Working f Number	Depth of Field
0	10.56	11.03	11.52	0.904	0.022	23.03	0.97
87	11.22	11.99	12.81	1.055	0.0305	19.74	1.59
125	12.72	13.75	14.85	1.137	0.0367	18.3	2.14
153	14.73	16.07	17.52	1.207	0.0431	17.23	2.79
177	17.46	19.20	21.12	1.274	0.0508	16.32	3.66
198	21.06	23.38	25.95	1.339	0.0601	15.53	4.89
217	25.93	29.07	32.65	1.403	0.0721	14.81	6.73
234	32.44	36.84	42.00	1.467	0.0878	14.16	9.56
250	41.86	48.40	56.39	1.532	0.1104	13.55	14.53
265	56.19	66.78	80.58	1.598	0.1456	12.98	24.39
279	79.89	99.52	128.19	1.666	0.2073	12.45	48.29
292	124.77	171.00	258.34	1.734	0.3406	11.95	133.57
300	185.08	293.14	628.44	1.779	0.5672	11.65	443.36
306	281.80	595.15	infinity	1.814	1.1266	11.46	infinity
308	339.18	893.01	infinity	1.826	1.6780	11.36	infinity
310	424.45	1764.18	infinity	1.838	3.2904	11.27	infinity
311	484.51	3400.26	infinity	1.844	6.3184	11.23	infinity
312	563.94	44124.55	infinity	1.850	81.686	11.23	infinity

The ZEMAX-based model is optimized on RMS spot size at a given focus distance. All linear dimensions are in millimeters; 306 is hyperfocal focus, 300 is good for TEGA images at closest distance, 312 is infinity focus.

*These measurements are the geometric depths of field based on 1 pixel blur.

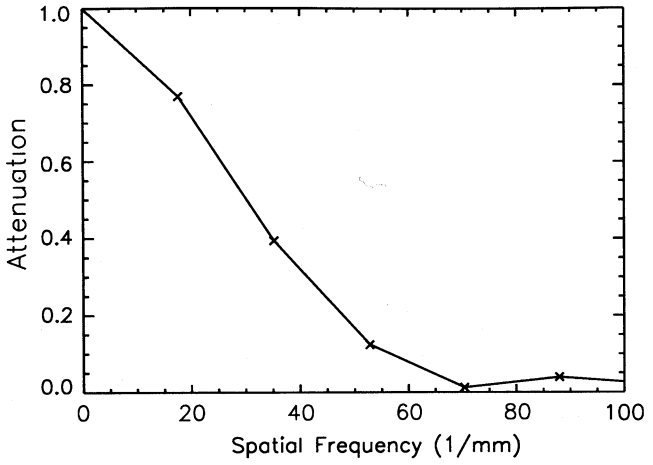

Figure 6. The RAC horizontal polychromatic modulation transfer function, 10:1 test, target 90 mm from camera.

a significant difference in the focus distance for some positions.

4.7. MTF

The RAC modulation transfer function (MTF) (Figure 6) was measured in the laboratory by taking images of unresolvable slits in three orientations: horizontal, vertical, and at a 45° angle. By stepping the slits in small increments we acquired the system line spread function (LSF). Taking the Fourier transform of the LSFs produces one-dimensional system MTFs. From these measurements it was determined that the RAC exhibits moderate aliasing because of the 23 μm pixel pitch. However, because of the spreading of the system response function with light of longer wavelengths, aliasing will be reduced when the scene radiance consists of primarily red to near-infrared light.

5. Sample Images

5.1. Overview

Extensive image series were taken in the laboratory to optimize the illumination and to develop data optimization and compression algorithms. A few samples demonstrate the capability of the RAC. In addition, the RAC was also used in a field test in the Mojave Desert to gain experience with and refine the analytical methods.

5.2. Images in the Mojave Desert

A prototype model of the RAC was tested in the Mojave Desert near Baker, California, on February 18-19, 1999. The test consisted of mounting the RAC on a simulated RA forearm, 72 cm from the nominal elbow. The scoop and Soil Temperature Probe (STP) were included, but the full RA was not. Several modes of imaging were tested.

First, the RAC obtained a 360° panorama of the horizon. The arm was rotated in 12° steps between images. This is about 1/4 of the RAC field of view, allowing creation of separate panoramas from the left-quarter frame and the right-quarter frame of the RAC images. The utility of the scheme was that the 12° steps produced little parallax error in the resulting mosaic despite the location of the RAC 72 cm from the axis of rotation, and the left side and right side, once registered, formed a stereo pair with a 40-50 cm baseline. The mosaic of left-quarter frame views is shown in Figure 7.

Second, the RAC was panned across the RA

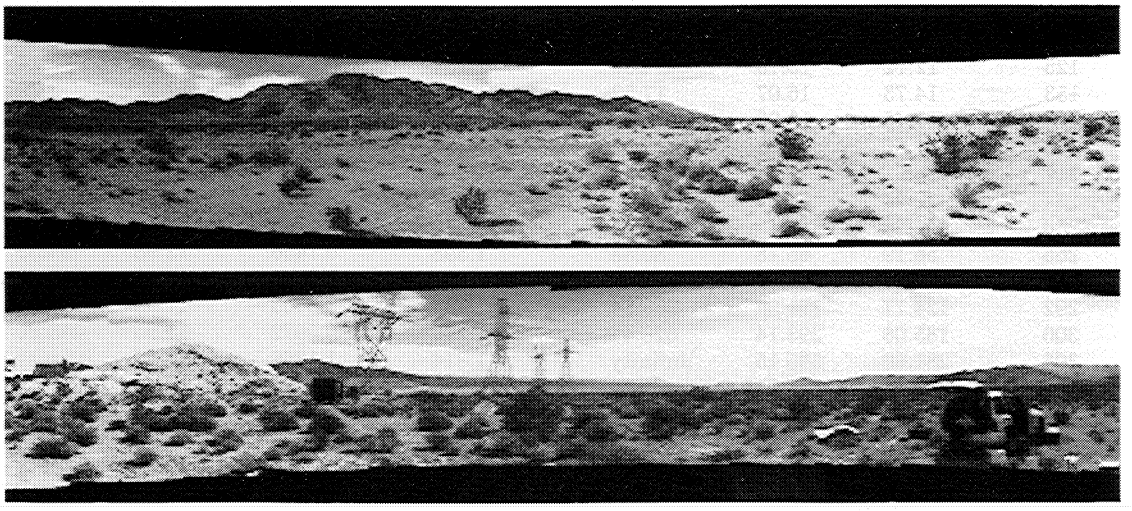

Figure 7. The Mohave Desert near Baker, California. This mosaic was created from 30 quarter frame RAC images, geometrically corrected and corrected for variations in brightness due to the partly cloudy day. The camera was slightly tilted down toward the workspace, resulting in the sine-wave pattern in the image. The bottom section of the panorama is the continuation of the right side of the top section.

Figure 8. The trench after the first dig to 10 cm depth.

workspace. A technique similar to that for making stereo pairs in the horizon set was used to make stereo pairs in the workspace data set. As part of the field test these images were used to decide where to dig a trench.

Third, during the process of digging the trench the RAC was used to document the trench itself and the pile of tailings. The trench at 10 cm depth is shown in Figure 8. Images of scoops of dirt were attempted, but the days were extremely windy, and dirt blew out of the scoop and debris blew into the trench. Instead, samples of the trench were collected and returned for laboratory analysis.

5.3. Images in the Laboratory

Soil samples were collected from surface fines, from surface pebbles, and from several depths in the trench. These were imaged in the laboratory with red, green, and blue LEDs for illumination (the setup is not identical to the Mars Polar Lander RAC but is qualitatively similar). To obtain color images, the sample was imaged first in ambient light (quite dark in the laboratory), then illuminated by each of the three colors. The ambient image was subtracted from the color images, which were then displayed in red, green, and blue channels. In addition, color targets were imaged for color calibration, as the lamps were not quantitatively identical to the flight model.

Plate 3 shows a sample of fines from the surface, imaged at close focus (10.5 mm distant and 25 μm pixel^{-1}). Plate 4 shows the effect of focal distance: the two images are at close focus, as above, and at 16 mm (46 μm pixel^{-1}). Other images were acquired with the scoop tilted away from the camera head, allowing viewing of contents deeper in the scoop (Plate 5). The illumination proved to be more uneven in this case.

6. Algorithms for Optimization of Data Taking

As discussed above, one of the primary applications of the RAC is to document the sample of the Martian soil that is to be delivered to TEGA for further analysis. Starting with the highest resolution 1:1 lens position, images at 11 positions are required to entirely cover the inside of the scoop (180 mm length). To obtain spectral information, three images have to be taken at each of these positions. The total of the 33 images translates to about 50 Mbits of data to be downlinked for each scoop content. This data volume is of the same order as the total expected for daily transmission. Clearly, there is a strong need to optimize RAC operation in this respect. Since compression of individual images solves the problem only partially, two algorithms, "active focus" and "depth of focus", are included in the lander's computer software to reduce the data volume without significant loss to the resultant science. Both of the algorithms return one image in each color instead of 11. A full discussion of these algorithms is beyond the scope of the present paper and will be reported on independently. Here, only a brief description and a few examples of the performance of these algorithms are given.

The active focus algorithm simply decides which of the images in the sequence is in best focus. The quality of the focus is obtained by calculating the total contrast in the image, defined as the sum over all pixels of |pixel - pixel above| + |pixel - pixel to left| divided by the sum of all pixels. The image in the sequence obtained at various focus positions with the highest sum is judged to be the best and is stored for downlink. This algorithm is very robust and performs well with most sceneries. The only type of scene which may cause some difficulties is one in which the scoop content forms a nearly plane surface at some inclination to the optical axes. This case is, however, very unlikely.

The depth of focus algorithm is much more complex. Its objective is to choose which pixels in each image sequence taken at different foci are in best focus and then create one composite image with only the best focus pixels. To accomplish this, the algorithm first creates synthetically blurred duplicates of the first and last images in the sequence, which are then added to the sequence list. This step is required because of the RAC's limited range of focus adjustment. Next the algorithm

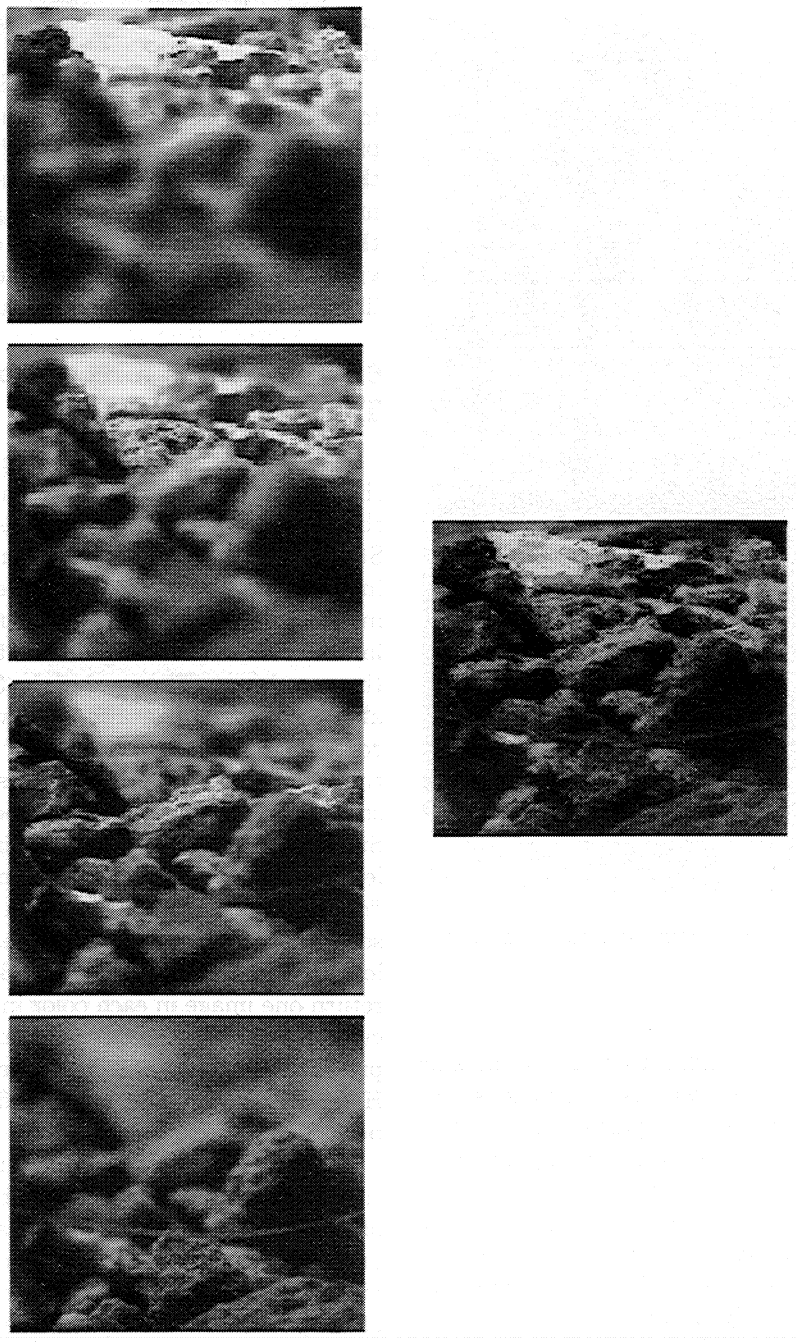

Figure 9. An example of the application of the depth of focus algorithm. The four images on the left are combined by the algorithm to produce the composite image on the right.

geometrically scales each image to the scale of the closest focus position (this implies subframing of the images at further positions so that the total pixel count on the rescaled images remains the same). In the current algorithm several different rescalings are tried, and the one that gives the best "fit" to the previous image is used. Then the images are radiometrically scaled relative to the working f number at the closest focus position. Finally, each pixel in the scene is evaluated across all the images to determine which image contains the maximum or minimum DN value for a given pixel. If the image contains the maximum or minimum DN value, the pixel value from exposures taken before and after are inspected to determine if they are both higher or both lower than the extremum pixel. When they are, that pixel is determined to be in focus and is written out to the final composite image. An example of a result obtained with the depth of focus algorithm is shown in Figure 9.

The depth of focus algorithm not only produces one good focus, composite image but also provides a record of the image from which each pixel in the composite

image originates. This feature is included in the flight software. The information is stored as a 256×512 array where each element contains the original image number for each pixel in the composite image. Using this information and the focus motor step data, it will be possible to calculate distances to each object in the composite scene.

Testing found the depth of focus algorithm to perform quite well for the typical scenes that the RAC will encounter when imaging the contents of the RA scoop. In some instances, though, the algorithm may not choose the optimum focus pixel. This has been seen to occur when objects in the foreground are very dark or very bright and are tall enough that they block the view of the rear of the scoop. The result is an easily recognizable 2-4 pixel halo surrounding the objects in the composite image. Although a minor degradation of the image, the manifestation of this effect can momentarily make images difficult to interpret.

7. Summary

The RAC is designed to minimize the mass at the wrist of the RA. Limits to the optimization of the design are set by the required heritage of existing components such as the detector packaging and the SHB. Hardly any concessions are made in respect to its performance. The RAC achieves 1:1 macro images in color with a resolution of better than 50 μm and at the same time can be used as a backup for SSI to take panorama and stereo images of the lander surroundings. The dynamic range within its images is based on the quality of the detector and the 12 bit A/D conversion that provide data with excellent signal-to-noise ratios. In fact, the very same camera will also fly on the (next) lander of Mars Surveyor 2001.

On the basis of its extensive capabilities, RAC will make major contributions to achieving the demanding science objectives of the MVACS payload.

Acknowledgments. The concept of the Robotic Arm Camera could be considerably improved above the original level described in the MVACS proposal by a synergistic, inspiring, and fruitful cooperation of dedicated experts on both sides of the Atlantic Ocean. We joyfully acknowledge the support and expertise of team members at MPAE: J. Nitsch for being involved in the electronics board layout and production, H. Schüddekopf for putting together the SHB and other delicate details, and K. Eulig for testing many CCDs; and at UofA: J. Bell for providing electronics engineering support and C. Shinohara for software design and support. P. Rüffer at Institut für Datenverarbeitung of the University of Braunschweig supported the data compression software effort. This research was supported in part by Deutsche Forschungsanstalt für Luft- und Raumfahrt (DLR) grant 50 QM 9630.

References

Bonitz, R.G., et al., The MVACS Robotic Arm, *J. Geophys. Res.*, this issue.

Boyton, W.V., et al., The Thermal and Evolved Gas Analyzer: Part of the Mars Volatile and Climate Surveyor integrated payload, *J. Geophys. Res.*, this issue.

Kramm, J.R., N. Thomas, H.U. Keller, and P.H. Smith, The CCD imager for the Mars Pathfinder and Mars Surveyor cameras, *IEEE Trans. Instrum. Meas.*, 47(5), 1112–1118, 1998.

Reynolds, R.O., and H. Hartwig, Design of a robotic arm camera for the Mars Surveyor Program, *Proc. SPIE Int. Soc. Opt. Eng.*, 3132, 68–77, 1997.

Rüffer, P., F. Rabe, and F. Gliem, Enhancement of IMP lossy image data compression using LCT, *JPL Publ.*, 95/8, 93–99, 1995.

Smith, P.H., et al., The Imager for Mars Pathfinder experiment, *J. Geophys. Res.*, 102, 4003–4025, 1997.

Smith, P.H., et al., The MVACS Surface Stereo Imager on Mars Polar Lander, *J. Geophys. Res.*, this issue.

Tomasko, M.G., et al., The Descent Imager/Spectral Radiometer (DISR) aboard Huygens, in *Huygens: Science, Payload and Mission, Eur. Space Agency Spec. Publ. ESA, SP-1177*, 109–138, 1997.

M. Fernandes, H. Hartwig, H.U. Keller, D. Koschny, R. Kramm, W.J. Markiewicz, and N. Thomas, Max-Planck-Institut für Aeronomie, Max-Planck-Strasse 2, 37191 Katlenburg-Lindau, Germany. (markiewicz@linmpi.mpg.de)

B.J. Bos, M.T. Lemmon, R. Marcialis, C. Oquest, R. Reynolds, P.H. Smith, R. Tanner, and J. Weinberg, Lunar and Planetary Laboratory, The University of Arizona, Tucson, AZ 85721.

D.A. Paige, Department of Earth and Space Sciences, University of California, Los Angeles, CA 90095-1567.

(Received June 18, 1999; revised October 20, 1999; accepted November 1, 1999.)